Patan Pragya *(Volume: 14, Number: 1, 2025)* *ISSN 2594-3278*

Received Date: April, 2025 Revised: May, 2025 Accepted: June, 2025

Laser-Scatter Analysis of Micro Particles in Carbon Quantum Dot Suspensions Using Droplet Ball-Lenses

Surendra Hangsarumba[a], Kishori Yadav[a], Suresh Prasad Gupta[a], Santosh Kumar Das[a]*, Saddam Husain Dhobi[a]*

[a] Department of Physics, Patan Multiple Campus, Tribhuvan University, Patandhoka, Lalitpur-44700, Nepal

*Corresponding Authors: saddam@ran.edu.np/dassantosh29@gmail.com

Doi: https://doi.org/10.3126/pragya.v14i1.90725

Abstract

Laser assisted optical microscopy of the carbon quantum dot (CQD) droplets is a new type tool to image micro- and nano-size structures in high resolution. The ball-lens method from which we sensed the size of objects that were encapsulated inside a hemispherical CQD droplet was also used for characterizing optical functionality of the CQD droplets as micro-lenses and their performance to detect particles at microscopic scale in suspended nanoparticles. Green light at 532 nm was focused by hemispherical CQD droplets (diameter 0.003 m) and magnified images were generated on a screened positioned 0.74 m away. The results of FTIR and XRD analyses corroborated the heterogeneous nature of CQDs that contain oxygenated, nitrogenated and aromatic domains resulting strong photostability and optical responsiveness. The average image size of the 17 measurements, is 0.01756 m in diameter, which corresponds to an estimated object size of about 75.310^{-6} *m; optical features such as these most probably correspond to clusters of CQDs or residual impurities rather than individual nanoparticles and suggest that our approach may be sensitive to micro-scale entities. The limitation is that it cannot distinguish individual quantum dots, and nonspecific droplet-induced distortions can lead to aberrations. The innovation for our method is the facile and low-cost implementation of CQD droplets as micro impurity magnifying glasses, which provides valuable perspectives in material characterization and quality control.*

Keywords: carbon quantum dots, micro-lenses, laser microscopy, image magnification, impurities, optical characterization

Introduction

Combining the capabilities of lasers with those of optical microscopy has revolutionized high-resolution imaging, providing unsurpassed levels of precision in biological and materials science. Laser-based microscopes use converging lenses to image coherent light onto a microscopic sample, and therefore achieve diffraction-limited spots for selective excitation. When integrated with a fluorescent probes, for example, CQDs, these nano-systems improve spatial resolution, signal to noise ratio and light–matter interaction (Das et al., 2024). This has the advantages of avoiding out-of-focus glare and low depth discrimination encountered in conventional brightfield microscopy. Type : mode Confocal and multiphoton microscopy, which pass through the actual specimen only a small fraction of the light used for illumination, operated by very tightly focused laser illumination in which optical sectioning is achieved with both fluorescence (Han et al., 2009; Ye et al., 2015). Frequency-doubled green lasers at 532 nm are popular because of the compatibility with fluorophores, reduced phototoxicity, and maximum detection sensitivity of silicon-based devices leading to an increase in imaging speed and contrast.

Although great progress has been achieved, there remain research challenges in the field of converging-optics, laser-assisted microscopy. Even then, many conventional configurations still suffer from spherical aberration in high-performance deep imaging of highly heterogeneous samples. Accurate positioning of the laser beam with respect to the optical axis of the converging lens still represents a major technical challenge, and this is even more evident in multimodal or dual-wavelength systems (De Vito et al., 2015). Incorporating fluorescent labels, such as CQDs, into the above systems could offer higher signal-to-noise ratio, better imaging flexibility and adjusted fluorescence afterglow as well as good biocompatibility and photostability. However, the previous CQDs based fluorescence imaging (Das et al., 2024; Tian et al., 2020) rarely considers the challenges in deep tissue or sample thick imaging region with strong optical aberration. To overcome these restrictions, the application of adaptive correction methods using deformable mirrors or wavefront shaping by computer is becoming ever more popular for dynamically adapting to aberration caused by a refractive index mismatch. New technologies additionally incorporate machine-learning algorithms toward maximizing focal spot quality at the time of imaging, and automatic drift correction during prolonged imaging sessions (Yano et al., 2016). Compact and economical platforms equipped with one off-the-shelf converging lens-based- aligned diode pumped solid state green laser in conjunction CQDs allow a higher contrast without using expensive fluorophores, making high-quality microscopy more affordable for resource-limited condition (Ka at al., 2025)

Laser-assisted microscopy with converging lenses presents broad-ranging relevance for applications including cell biology, neuroscience and semiconductor inspection. High-NA objectives and advanced converging lenses allow subcellular imaging at the nanometer level, thus enabling observations of intracellular dynamics and molecular interactions (Tserevelakis et al., 2023). Using these systems in combination with fluorescent probes such as carbon quantum dots CQDs improves contrast, photostability and biocompatibility, producing bright and stable fluorescence under low light or long-term imaging (Das et al., 2024). For example, in industrial processes, focused green lasers can be used for non-contact metrology and defect inspection. Green 532 nm lasers give better contrast for fluorescence lifetime imaging and Raman spectroscopy (Matsutani, 2025; Martin et al., 2019). Improved focusing enhances the photon collection efficiency and increases sensitivity in single-molecule detection. The incorporation of laser physics, optics and QDs facilitates advancement in super resolution as well as light-sheet microscopy for biological and bioimaging applications.Green laser excitation with focusing optics enables more sensitive microscopy. Laser-scanning confocal microscope with high pinhole alignment and lens for optimal sectioning. A laser-scanning confocal microscopy was applied in the early investigations (Han et al., 2009; Ye et al., 2015). Subsequent studies investigated polarization-preserving lens systems in order to retain excitation control in anisotropic samples (De Vito et al., 2015). In bioimaging, CQDs were doped as fluorescent probes which could exhibit photobleaching resistance, précised emission tunability and good biocompatibility to perform convincing imaging under weak lighting or for a long time (Ou et al., 2021). Focused 532nm is an indispensable tool for optogenetic studies that permit localized mechanical probing or neural activation (Sebastian et al., 2015; Zhang et al., 2024). Reconstruction of coherence factor and resolution enhancement with laser illumination (Chung et al., 2016). Hybrid systems coupling laser-induced breakdown spectroscopy (LIBS) and microscope optics also attain micrometer-resolution elemental mapping (Alfarraj et al., 2020). These developments, facilitated by CQDs, can extend applications from bioimaging to analytical materials characterization.

Methodology

Materials: A 532 nm green laser (100 mW) was used as the monochromatic light source in the scattering experiments. CQDs were prepared in lab by heating a mixture of citric acid and urea in a micro-oven, as reported by Dhobi et al. (2025). The obtained CQDs were further centrifuged at 16,000 rpm for 120 s to take away the agglomeration. The dots purified were gently deposited on a burette (50 ml) in Figure1. With the help of a high-precision control, the tip of burette was adjusted to make hemispherical CQD droplet that became the scattering medium for incoming laser beam. This architecture allowed investigation of well-controlled laser CQD light interactions.

Experimental system: A hemispherical CQD droplet of 0.003 m in diameter was placed between a vertical screen (with scale 0.25 m) and a green laser as monochromatic light led source. The droplet was held stable by a burette and its fine controlled head, the support of the burette adding to its placement stabilization. The laser was fixed with a bench vise at exactly 0.1 m from the droplet center. A laser beam with diameter 0.003 m passed through the CQD droplet and the scattered patterns were recorded on a screen located 0.74 m from the droplet. The spotted small speckle-like structure shown was not real speckles but magnified images of the micro-object inside the droplet (Delord et al., 2017). Functioning as the converging lens, the hemispherical droplet yielded inverted magnified images at a certain distance of observation leading towards effective magnification of structures residing inside them (Nagelberg et al., 2017). The experiment was conducted at Department of Physics, Patan Multiple campus, Lalitpur, Nepal.

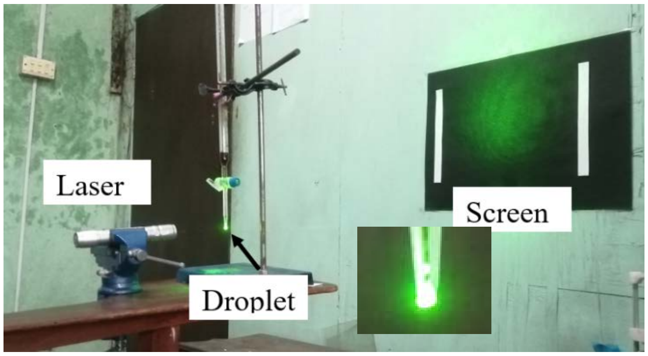

Figure 3. ***Experimental Setup for the Laser Scattering on CQD Hemispherical Droplet***

Refractive Index (R.I.): RI of the CQDs solution was found by a rotating spectrometer in combination with hollow prism located at Patan Multiple Campus. 40 mL of the CQDs solution was added to the hollow prism and both its minimum deviation angles were recorded with and without the sample. R.I. is determined by using famous Snell's law (Hecht, 2017);

$$R.I. = \frac{Sin\frac{A+D_m}{2}}{Sin\frac{A}{2}} \tag{1}$$

Where: A= Angle of Prism; D_m= Minimum deviation

Measurement of image: Captured images were processed using an ImageJ software (as illustrated by figure 2) containing a screen calibrated to the vertical distance of 0.25 m. Several images from various views were collected; seventeen observations in total provided poling data with statistical validity. The data were then fit to a Gaussian distribution to obtain the average diameter and area of the image structures. This technique allowed a quantitative description of magnified images by the CQD droplet, yielding consistent values on size and spatial distribution.

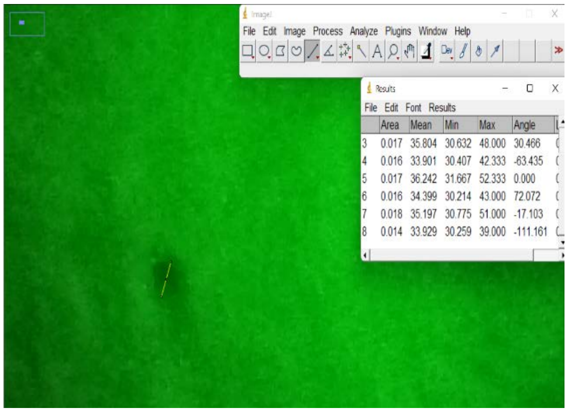

	Area	Mean	Min	Max	Angle
3	0.017	35.804	30.632	48.000	30.466
4	0.016	33.901	30.407	42.333	-63.435
5	0.017	36.242	31.667	52.333	0.000
6	0.016	34.399	30.214	43.000	72.072
7	0.018	35.197	30.775	51.000	-17.103
8	0.014	33.929	30.259	39.000	-111.161

Figure 4. ***Image Analysis of the scattered pattern***

In experiments, spherical droplets can function as ball lenses, allowing the formation of images of small objects (Maslov et al., 2023). For a spherical ball lens, a common paraxial estimate for the focal length is expressed as:

$$f \approx \frac{nR}{2(n-1)} \tag{2}$$

where n is the refractive index of the droplet and R its radius. Also, the simultaneously small spherical aberration (Perigger et al., 1997) is not considered here in this study. When the droplet is illuminated, it forms an intermediate image. The thin-lens equation governs the relationship between the focal length, object distance, and image distance (Hecht, 2017):

$$\frac{1}{f} = \frac{1}{v} + \frac{1}{u} \tag{3}$$

The linear magnification from the object to the intermediate image is given by (Hecht, 2017):

$$m_1 = \frac{v}{u} \tag{4}$$

But for ball like lens $v \gg f$,

$$\mathrm{M} = \frac{v}{f} \tag{5}$$

Now the object size is obtained with formula:

$$D_{Object} = \frac{D_{Image}}{M} \tag{6}$$

These theoretical frameworks are taken for estimating object sizes using a spherical droplet as a lens, independent of numerical values, and under the paraxial approximation.

Results

FTIR and XRD analysis: The FTIR spectrum of CQDs prepared was presented in Fig. 3a and the peak positions were shown in Table 1, several characteristic absorption bands correlated to functional groups that can be found in sensing and optical properties. The band at about 641 cm^{-1} is assigned to the P–O, S–O, aromatic C–H or silicate vibrations. A strong peak at around 1177 cm^{-1} is attributed to O–C bonds from partially oxidized phosphate groups indicating a structural polymerization of within the carbon matrix. The conjugated π-domains that allow electron delocalization are thus indicated by the C=C stretching band around 1721 cm^{-1}. Nitrogen is also incorporated as reflected in the C=N vibration at around 1585 cm^{-1}. Moreover, the band at 2938 cm^{-1} represents stretching from CH_3 and CH_3 moieties which suggest aliphatic chain that contributes surface polarity and interaction sites. The characterized of CDQs, XRD and FTIR was conducted at Nepal academy of science and technology (NAST), Lalitpur Nepal.

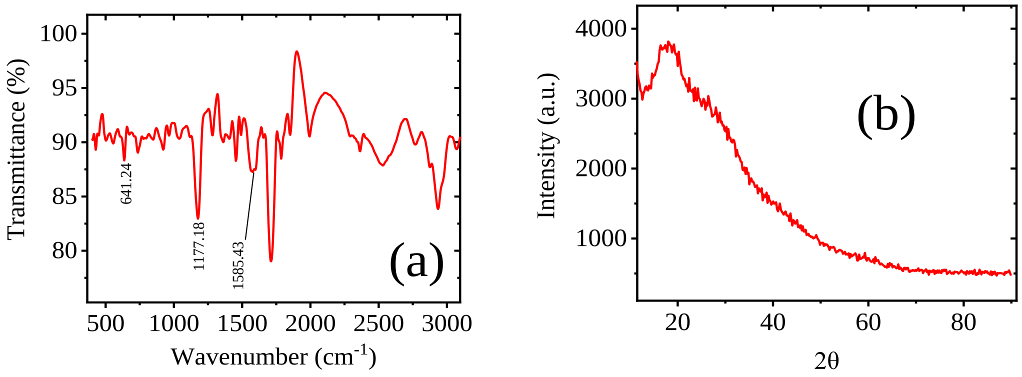

Figure 5 (a) ***FTIR analysis and*** *(b)* ***XRD analysis of synthesized Quantum dots***

XRD pattern of the prepared CQDs (Figure 3b) show characteristic peaks at 14.41°, 16.02° and 18.00° associated with organic crystal phases including $C_{20}H_{28}O_4S$ and K_4WO_5. The lack of intense inorganic and metallic peaks implies that the material is dominantly organic, with aliphatic and aromatic domains. Nitrogen doping via the urea modified precursor dopes defect sites by and strengthens π-conjugation, thereby helping to semiconductor the behavior as well as improve carrier mobility. These structures facilitate rapid charge transfer and good responsiveness to external factors. Together with FTIR, the results confirmed that it had a heterogeneous, but functionalized structure rich in oxygenated, nitrogenated and aromatic groups which might offer high optical responsiveness eigen-states dependent emission behavior and high adsorption capacity for future sensing applications.

Table 1 ***Experimental and referenced FTIR peak analysis***

Possible assignment	Observed wavenumber (cm^{-1})	Reference wavenumber (cm^{-1})	Refrence
–P–O, –S–O, and aromatic –CH stretching or Silicate	641.24	474.68-661.77	(Mansour et al., 2022)
–O–C links of the organic phosphate groups	1177.18	1242.68	
C=C stretching	1721.05	1546.33,1656.51 3279.90	
Asymmetric CH3 & symmetric CH2 stretching	2938.71	2854.48	

Size of the Image: The distribution of measured image size from all 17 sets is shown in Figure 4. We can observe in the histogram that most of the images are concentrated between 1.6 cm and 2.0 cm, with a central tendency around 1.756 cm computed from mean and median values. The minimum and maximum sizes we observe are 1.118 cm and 2.324 cm, respectively, indicating that the data span a moderate range. The standard deviation of 0.275 cm also supports this variation, whereby although the majority of the measurements fall close to the mean, there is variability on both low and high sides. The histogram with the smooth curve fits a Gaussian, suggesting that the differences in size are determined mainly by random measurement errors instead of systematic discrepancies. This central peak provides a robust estimate to the typical image size that one would expect at these experimental conditions. The histogram obtained from the ImageJ analysis of the given data exhibits an approximately Gaussian distribution, with values spanning from about 1.12 cm to 2.32 cm. The fitted Gaussian curve shows a mean value and a standard deviation, indicating that most data points are concentrated near the central value with moderate dispersion. The close agreement between the histogram and the Gaussian fit suggests that the data are normally distributed and mainly influenced by random variations, reflecting uniformity and stability in the measured parameter. Nearly 65–70 % of the data lie within ±1σ of the mean, while about 95 % fall within ±2σ, consistent with normal distribution behavior. This percentage-based spread confirms that most values are closely clustered around the mean, reflecting good uniformity and minimal extreme variation in the measured parameter.

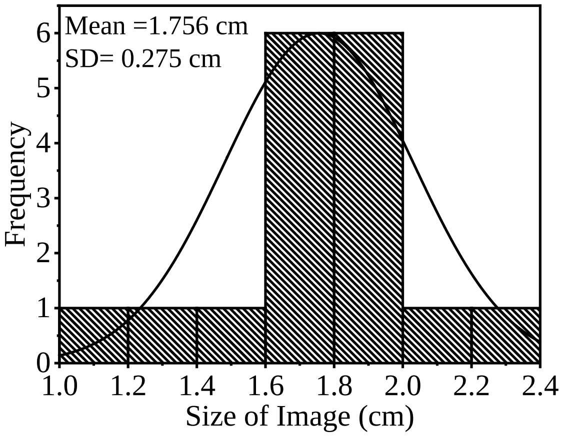

Figure 6. ***Distribution on measurement of the Image size***

The normality assumption is supported as the data show a symmetric distribution with respect to the mean, which roughly coincides with median 1.756 cm. The edges (1.0–1.2 cm and 2.2–2.4 cm) of both histograms have shorter bars, meaning that extreme image sizes are less common. This frequency map indicates that experimental parameters (droplet uniformity, laser alignment, measurement accuracy) do not significantly contribute to outlier appearance. Taken together, Figure 4 nicely illustrates the stability and robustness of the size measurements on the images by simultaneously reporting central tendency and dispersion. A statistical basis is important to assess the reproducibility of any experimental setup and validate the image formation process in this study.

According to Figure 5, the distribution of image area is nearly normally distributed or bell-shaped centered around a mean value of 3.501 cm^2. The number of samples is 17, its standard deviation is 1.139 cm^2, suggesting a moderate spread of the values around the mean. The smallest and largest areas recorded are 1.118 cm^2 and 5.387 cm^2 respectively, which indicates a large range. The median very closely corresponds to the mean, and that further indicates how symmetric the distribution is. This central tendency is also supported by the histogram, where most of the images are concentrated in middle area categories and degrades as we move away from that area into small and large regions. This implies that majority of the images are of moderately same size and with few exceptions at both ends.

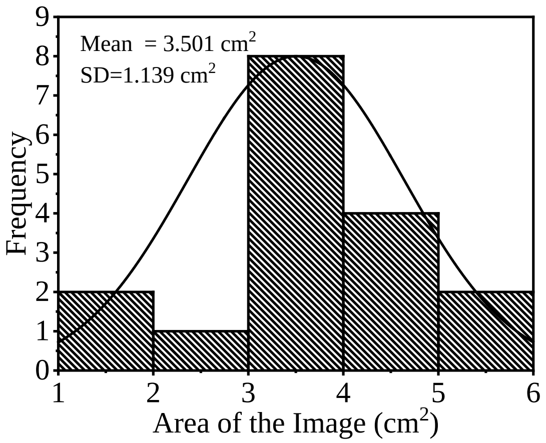

Figure 7. ***Area Distribution of the Images***

The symmetry and the mean/median proximity would hint that there is no strong skew, i.e., we did not under-sample particularly small or large images from the image area distribution. The low standard deviation suggests most images tend to stay close the average size with some natural variation that is expected. This consistency is important for maintaining the validity of later analyses by minimizing image size as a confounder. Lastly, the area distribution is robust as to be used as an argument for further research without enforcing some statistical transformation to normalize skewness.

The average size of the micro particle: The R.I. n of QDs is calculated and is obtained to be 1.317. Using the information as provided in methods, the size of the object inside the droplet is obtained as:

$$f = \frac{1.317 \times 0.0015}{2(1.317 - 1)} \tag{7}$$

$$f = 0.00317\ m \tag{8}$$

Magnification (M) for the ball lens is *v/f* = 0.74/0.00317=233.13 then the size of the object is:

$$D_{Object} = \frac{D_{Image}}{M} \tag{9}$$

$$D_{Object} = 75.3 \times 10^{-6} m \tag{10}$$

From this, it was deduced that the droplet would behave as a strong converging lens having focal length of nearly 0.00317 m and considering measured distance to be formed on the screen from image probe, we got magnification as nearly 233 which means projected image on the screen was hundreds of times greater than actual size of object inside droplet. By taking the observed size of the image and dividing it by this magnification factor, we were able to get the real size of that internal object, which resulted in a value approximately equal to 75.3 $\times 10^{-6}$ m. Note also that the object which is measured inside the droplet does not represent a single quantum dot. With an average size of approximately 75.3×10^{-6} m, this is significantly bigger compared to typical carbon quantum dots that are generally between 2 and 10 nm. Hence, there are likely cluster of QDs or aggregates or even other kind of micro size impurities which were not completely removed from the centrifugation process resulting in what is observed. Although it was not possible to directly measure the size of individual quantum dots in this study, this optical imaging approach was successfully used to detect micro-sized particles distributed along with nano-materials. Gradient force measurements such as these reveal the existence of larger size features, e.g., remaining species or ensembles of them that might affect optical patterns/scattering. This methodology, therefore, can be a powerful technique for detection and characterization of micro impurities or clusters within the suspensions of nanoparticles, allowing information about sample purity and distribution to be obtained even if individual particle dimension cannot yet be determined.

Conclusion

In the current work, it has been shown that hemispherical shaped carbon quantum dot droplets can act as efficient micro-lenses and achieve magnification and imaging of embedded micro-structures. The use of a 532 nm green laser and accurate positions of droplets on the screen brought about clear, magnified images that were difficult to observe otherwise. FTIR and XRD characterizations indicated that the prepared CQDs have heterogenous and functional as well as oxygenated, nitrogenated, and aromatic domains for strong optical responsivity and photostability. These objects had a mean measured diameter of ~75.3×10^{-6} m, which is much larger than the average size of typical quantum dots and suggested that these observations correspond to clusters, aggregates or residual microscale impurities left after centrifugation but no single quantum dots. Though not used for direct determination of size, this technique allows detection of fine scale features associated with the nanoparticles giving some information about sample purity/aggregation and distribution. Overall, this work demonstrates a simple but powerful optical method to characterize micro impurities in nanoparticle suspensions for quality control and optical sensing of nanomaterials.

References

Das, S., Mondal, S., & Ghosh, D. (2024). Carbon quantum dots in bioimaging and biomedicines. *Frontiers in bioengineering and biotechnology, 11*, 1333752.

Tian, X., Zeng, A., Liu, Z., Zheng, C., Wei, Y., Yang, P., ... & Xie, F. (2020). Carbon quantum dots: In vitro and in vivo studies on biocompatibility and biointeractions for optical imaging. *International journal of nanomedicine*, 6519-6529.

KA, N., Poulose, A., P, A., AS, S., PN, P. K., & KS, P. (2025). Engineering Nanomaterials for Raman Bioimaging and Theranostics: Advances, Challenges, and Future Directions. *ACS omega*.

Han, Z., Chen, X. Y., & Ma, D. R. (2009). The Experimen- tal Technology and Application of Laser Scanning Confocal Micro- scope. *Science & Technology Information*, *19*, 27.

Ye, L. I., Huaping, H. U. A. N. G., & Peiqun, L. I. N. (2015). The fundamentals and techniques in laser scanning confocal microscopy. *Journal of Chinese Electron Microscopy Society*, *34*(2), 169-176.

Ou, S. F., Zheng, Y. Y., Lee, S. J., Chen, S. T., Wu, C. H., Hsieh, C. T., & Hsueh, Y. H. (2021). N-doped carbon quantum dots as fluorescent bioimaging agents. *Crystals*, *11*(7), 789.

De Vito, G., Canta, A., Marmiroli, P., & Piazza, V. (2015). A large-field polarisation-resolved laser scanning microscope: applications to CARS imaging. *Journal of Microscopy*, *260*(2), 194-199.

Yano, T. A., Tsuchimoto, Y., Mochizuki, M., Hayashi, T., & Hara, M. (2016). Laser scanning-assisted tip-enhanced optical microscopy for robust optical nanospectroscopy. *Applied Spectroscopy*, *70*(7), 1239-1243.

Tserevelakis, G. J., Tekonaki, E., Kalogeridi, M., Liaskas, I., Pavlopoulos, A., & Zacharakis, G. (2023, March). Hybrid fluorescence and frequency-domain photoacoustic microscopy for imaging development of Parhyale hawaiensis embryos. In *Photonics* (Vol. 10, No. 3, p. 264). MDPI.

Matsutani, A. (2025). Measurement of lens function of yeast cells using optical microscope and laser pointer. *Physics Education*, *60*(5), 055028.

Martin, M., Hamm, D., Martin, S., Allman, S., Bell, G., & Martin, R. (2019). Micro-laser-induced breakdown spectroscopy: a novel approach used in the detection of six rare earths and one transition metal. *Minerals*, *9*(2), 103.

Sebastian, T., Schultheiss, K., Obry, B., Hillebrands, B., & Schultheiss, H. (2015). Micro-focused Brillouin light scattering: imaging spin waves at the nanoscale. *Frontiers in Physics*, *3*, 35.

Zhang, X., Wu, Y., Cai, S., & Feng, G. (2024, March). Optical Manipulation of Fibroblasts with Femtosecond Pulse and CW Laser. In *Photonics* (Vol. 11, No. 3, p. 248). MDPI.

Chung, J., Lu, H., Ou, X., Zhou, H., & Yang, C. (2016). Wide-field Fourier ptychographic microscopy using laser illumination source. *Biomedical optics express*, *7*(11), 4787-4802.

Alfarraj, B. A., Alkhedhair, A. M., Al-Harbi, A. A., Nowak, W., & Alfaleh, S. A. (2020). Measurement of the air bubble size and velocity from micro air bubble generation (MBG) in diesel using optical methods. *Energy Transitions*, *4*(2), 155-162.

Nagelberg, S., Zarzar, L. D., Nicolas, N., Subramanian, K., Kalow, J. A., Sresht, V., ... & Kolle, M. (2017). Reconfigurable and responsive droplet-based compound micro-lenses. *Nature communications*, *8*(1), 14673.

Delord, T., Nicolas, L., Schwab, L., & Hétet, G. (2017). Electron spin resonance from NV centers in diamonds levitating in an ion trap. *New Journal of Physics*, *19*(3), 033031.

Hecht, E. (2017). *Optics* (5th ed.). Pearson. https://www.pearson.com/en-us/subject-catalog/p/optics/P200000006793/9780137526420

Maslov, A. V., Jin, B., & Astratov, V. N. (2023). Wave optics of imaging with contact ball lenses. *Scientific Reports*, *13*(1), 6688.

Parigger, C., Tang, Y., Plemmons, D. H., & Lewis, J. W. (1997). Spherical aberration effects in lens–axicon doublets: theoretical study. *Applied Optics*, *36*(31), 8214-8221.

Dhobi, S., Hangsarumba, S., Kamat, R. K., Yadava, K., & Gupta, S. P. (2025). Synthesis of carbon quantum dots and their optical properties under various conditions. *Jurnal Fisika, 15*(2), 51–65. https://doi.org/10.15294/jf.v15i2.33311